

Machine learning-based automatic identification and diagnosis of dental caries and calculus using hyperspectral fluorescence imaging

Cheng Wang^{a,c}, Rongjun Zhang^a, Xiaoling Wei^b, Le Wang^a, Wenqian Xu^{a,c}, Qi Yao^{a,c,*}

^a Department of Optical Science and Engineering, Academy for Engineering and Technology, Fudan University, Shanghai 200433, China

^b Department of Endodontics, Shanghai Key Laboratory of Craniomaxillofacial Development and Diseases, Shanghai Stomatological Hospital, Fudan University, Shanghai 200001, China

^c State Key Laboratory of Applied Optics, Changchun Institute of Optics, Fine Mechanics and Physics, Chinese Academy of Sciences, Changchun 130033, China

ARTICLE INFO

Keywords:

Hyperspectral fluorescence imaging

Machine learning

Dental caries

Calculus

Enhanced recognition

ABSTRACT

Purpose: Precise diagnosis and identification of early dental caries facilitates timely intervention and reverses the progression of the disease. Developing an objective, accurate and rapid caries and calculus automatic identification method advances clinical application and facilitates the promotion and screening of oral health in the community and family.

Methods: In this study, based on 122 dental surfaces labeled by professional dentists, hyperspectral fluorescence imaging combined with machine learning algorithms was employed to construct a model for simultaneously diagnosing dental caries and calculus. Model trained by fusion features based on spectra, textures, and colors with the integrated learning algorithm has better performance and stronger generalization capabilities.

Results: The experimental results showed that the diagnostic model's accuracy, sensitivity, and specificity for identifying four different caries stages and calculus were 98.6%, 98.4%, and 99.6%, respectively.

Conclusions: The proposed method can evaluate the whole tooth surface at the pixel level and provides discrimination enhancement and a quantitative parameter, which is expected to be a new approach for early caries diagnosis.

1. Introduction

Dental caries and periodontitis are both quite common oral diseases [1]. Dental caries is one of the most prevalent chronic diseases worldwide, affecting 60%–90% of schoolchildren and almost all adults [2]. Severe periodontitis affects approximately 10% of the world's population [3]. Subgingival calculus is considered a major cause of periodontitis, and successful periodontal treatment requires the complete removal of calculus [4,5]. Dental caries are the hard tissue localized damage to sensitive teeth due to acidic by-products produced by bacterial fermentation [6]. The non-mineralized oral biofilm containing many bacteria, human proteins, viruses, and food residue particles, forms calculus when mineralized by calcium phosphate inorganic salts [7]. The dynamic caries process consists of rapid alternating tooth demineralization and remineralization cycle. Suppose net demineralization occurs long enough for caries lesions to begin to appear. Early dental caries, which manifest clinically as white spots, can be stopped or even reversed with preventive measures or changing the causative

factors [8]. Therefore, early diagnosis of dental caries is very important.

However, the conventional clinical diagnostic methods of visual examination, palpation, and radiographic examinations have a higher risk of failing to detect early caries [9]. Consequently, many studies and methods have focused on the feasibility of utilizing optical and imaging-based methods for early caries detection, thus avoiding invasive surgical treatment of dental caries [10–14]. Fluorescence spectrometry and fluorescence imaging, including Quantitative Light-induced Fluorescence (QLF) and Laser-induced Fluorescence (LF), is a non-invasive, non-ionizing detection process [15]. When excited by violet-blue light, the healthy enamel will produce emission peaks in 480–510 nm. However, with the progress of caries disease, 1–2 increasing emission peaks will be produced in 590–705 nm [16,17]. Inorganic substances in sound tooth enamel contain fluorophores, which will emit green light when excited, while the tooth surface with caries contains bacterial metabolic by-products porphyrins, especially protoporphyrin IX which will emit red light with excitation [18,19]. The calculus contains many calcified plaques with high porphyrin content

* Corresponding author at: Academy for Engineering and Technology, Fudan University, Shanghai 200433, China.

E-mail address: yaoqi@fudan.edu.cn (Q. Yao).

<https://doi.org/10.1016/j.pdpdt.2022.103217>

Received 8 August 2022; Received in revised form 7 November 2022; Accepted 29 November 2022

Available online 30 November 2022

1572-1000/© 2022 Elsevier B.V. All rights reserved.

and can be detected similarly [4]. These are the theoretical bases for identifying caries stages and calculus by QLF or LF.

Much research on selecting excitation light source wavelengths, optimizing characteristic spectra and parameters, and quantifying color features has been presented to distinguish between different caries stages and calculus. Bahramian et al. compared the fluorescence spectra at three laser excitation wavelengths for healthy enamel, dentin, and carious dentin [20]. Ribeiro et al. employed the combined fluorescence ratio in the 480–500 nm and 620–640 nm spectral bands as a parameter to distinguish sound and carious tooth surfaces [21]. Chen et al. utilized the color features between caries and sound tooth surfaces to distinguish them [22]. Although spectral and color features can be useful for assessing caries and calculus, in practice, using only single-point spectra is time-consuming and laborious, and using fluorescence images can be difficult to distinguish because of the metamerism and the small color gamut displayed [23].

The International Caries and Detection Assessment System II (ICDAS II) is a 7-point scale (codes 0–6) clinical visual classification system for detecting and assessing all stages of dental caries development [24]. As a result of the 2008 American Dental Association Symposium, it was suggested that the ICDAS II codes could be combined into four categories indicating the different stages of caries progression [25]. Therefore, this paper classified dental specimens into five disease categories: ICDAS II 0, ICDAS II 1,2, ICDAS II 3,4, ICDAS II 5,6, and dental calculus.

Hyperspectral imaging (HSI) is a promising optical technology for medical applications that combines the advantages of spectral technology and digital imaging [26]. Some research is already applying hyperspectral techniques to diagnosing dental caries and calculus. Abdel Gawad et al. utilized hyperspectral imaging to provide a set of wavelengths that can be applied to diagnose white spots, calculus, and enamel caries lesions [27]. Usenik et al. employed Near-Infrared (NIR) hyperspectral imaging combined with multiple discriminant analyses to classify oral tissues [28]. They demonstrated the advantages of hyperspectral imaging applied to the evaluation and diagnosis of dental caries and calculus.

Machine learning is a powerful technique for recognizing patterns that can be applied to medical images and help doctors in medical diagnosis [29]. Song et al. utilized dual-modal images combined with deep learning to detect oral cancer [30]. Hur et al. identified caries in radiographs using five machine learning algorithms [31]. Hung et al. constructed a classifier to predict the presence of root caries by using several supervised machine learning methods [32]. To our knowledge, the identification and classification of caries stages and calculus using hyperspectral fluorescence imaging combined with machine learning has not been reported yet.

Given the need for accuracy in early caries identification, this paper proposes an image modeling method based on hyperspectral fluorescence imaging combined with machine learning. The spectral features, spatial texture features, and color features of each pixel are fused to build the model. This objective, accurate and rapid method of identifying and assessing caries stages and calculus is expected to provide a solution for early caries diagnosis.

The main contributions of this work are summarized as follows:

- (1) We propose an objective, accurate and fast method for the automatic identification of caries stages and calculus.
- (2) The fusion of three features, spectral, textural and color, proved to be more useful for the diagnosis of caries stages and calculus.
- (3) The performance of four common machine learning algorithms is evaluated, and the optimal model is obtained by combining fused features with integrated learning.
- (4) The diagnostic model proposed in this paper can evaluate caries stages and calculus on the entire tooth surface at the pixel level, while providing discrimination enhancement and parameter quantification.

The rest of the paper, structured as: Section 2, explains the material and methodological sections, which include Sections (2.1) tooth specimens. (2.2) experimental facilities. (2.3) original dataset establishment and image pre-processing. (2.4) feature fusion and machine learning algorithms. (2.5) model assessment. Section 3, explains the results and discussion which comprise Section (3.1) feature analysis, analyze the shortcomings and deficiencies of existing single-feature (spectral, color and characteristic bands) diagnostics. (3.2) model training process. (3.3) ablation study and comparison with other methods. (3.4) prediction process. (3.5) enhanced recognition and quantitative assessment. Section 4 concludes the paper.

2. Materials and methods

2.1. Tooth specimens

Eighty-three dental samples were obtained from the Department of Endodontics, Shanghai Stomatological Hospital, Fudan University. The procedures were conducted according to the ethical principles for medical research involving human beings as specified in the Declaration of Helsinki (2013 version) of the World Medical Association. This study was approved by the Medical Ethics Committee of Shanghai Stomatological Hospital (No. HKFLS2019003). Teeth were extracted for various types of oral diseases. Each tooth specimen has five tooth surfaces, including distal, occlusal, mesial, lingual, buccal [28]. Professional dental clinicians visually inspect these tooth surfaces, determine the area and stage of caries according to ICDAS II standards, and mark the calculus location. As listed in Table 1, one hundred and twenty-two tooth surfaces were finally divided into five classifications, labeled with caries area and stage: thirty ICDAS II 0, twenty-six ICDAS II 1,2, twenty-four ICDAS II 3,4, twenty ICDAS II 5,6 and twenty-two calculus, respectively. Dental samples were preserved in a 10% formalin solution which can retain most of the fluorescence effect [33]. Tooth samples were controlled for two weeks from extraction to completion of testing.

2.2. Experimental facilities

Fig. 1 shows the schematic diagram of the hyperspectral fluorescence imaging system, including an LED light source, dental specimen, high-pass filter, hyperspectral camera, and computer. The excitation source was a 405 nm LED (6 W), and the full width at half maximum was about 15 nm. Previous work had demonstrated that the 470–780 nm spectral

Table 1

. Number of tooth specimens, tooth surfaces, POIs, and pixel point intensity values.

Category	Number of tooth specimens	Number of tooth surfaces	Number of POIs	Number of spectral bands	Number of pixel point intensity values
ICDAS II 0	83	30	600	311 (470–780 nm, 1 nm interval)	186,600 (600 × 311)
ICDAS II 1,2		26	510		158,610 (510 × 311)
ICDAS II 3,4		24	470		146,170 (470 × 311)
ICDAS II 5,6		20	400		124,400 (400 × 311)
Calculus		22	440		136,840 (440 × 311)
Total		122	2420		752,620 (2420 × 311)

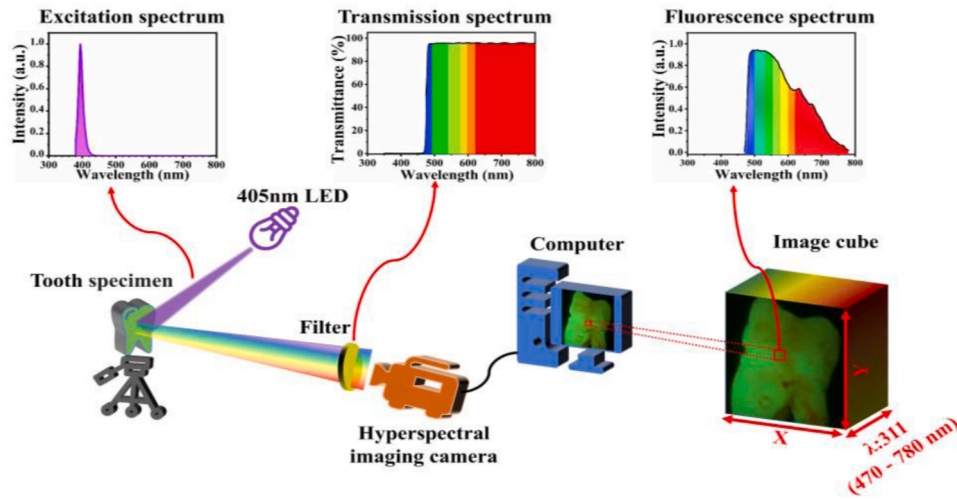


Fig. 1. Hyperspectral fluorescence imaging system schematic.

power distribution (SPD) is the best color-matched band for fluorescence imaging [34]. A high-pass filter at 470 nm was employed to filter the 405 nm LED spectrum and the dental specimen’s fluorescence spectrum in the 440–470 nm band. In our previous work it was concluded that the use of 470–780 nm filters facilitates the observation and diagnosis of dental caries [34]. The calibrated hyperspectral camera (SR-5000, TOPCON) captures the fluorescence spectrum of the dental specimen in the 470–780 nm band, displaying the fluorescence image on a computer with pre-installed software as well as obtaining image cubic data. The obtained image cubes had 1376×1024 spatial resolution and spectral information with a 1 nm interval in the 470–780 nm band. In addition, white RGB images of dental specimens are acquired by a smartphone, and fluorescent RGB images are acquired by the hyperspectral camera, as shown in Fig. 2(b). A dark room was used for the entire measurement, and the integration time was adjusted to ensure that a smooth and continuous spectrum was obtained. The spectral data were calibrated to exclude noise, pseudo-shadowing, and dark current interference [35].

2.3. Original dataset establishment and image pre-processing

The white RGB images were provided to the clinician for marking the caries locations and areas, which were used as the gold standard. 2420 Points of Interest (POIs) were extracted from 122 tooth surfaces according to the professional clinician’s labeling of tooth surface caries stages and calculus. 10 or 20 POIs were taken for each tooth surface, as shown in Table 1, and each POI contained 311 bands (470–780 nm, 1 nm interval). In total, 752,620-pixel point intensity values were obtained as the original dataset. In the image pre-processing stage, the methods of Principal Component Analysis (PCA), Otsu threshold segmentation, and Gabor texture feature extraction were employed. Since the dimensional information acquired by hyperspectral imaging techniques is usually much larger than the number of training samples available, dimension reduction was a common pre-processing step to avoid this curse of dimensionality. PCA has become a standard tool in hyperspectral image processing due to its simplicity, non-parametric, and effectiveness in extracting relevant information from HSI [36]. Otsu threshold segmentation was one of the most widely used image

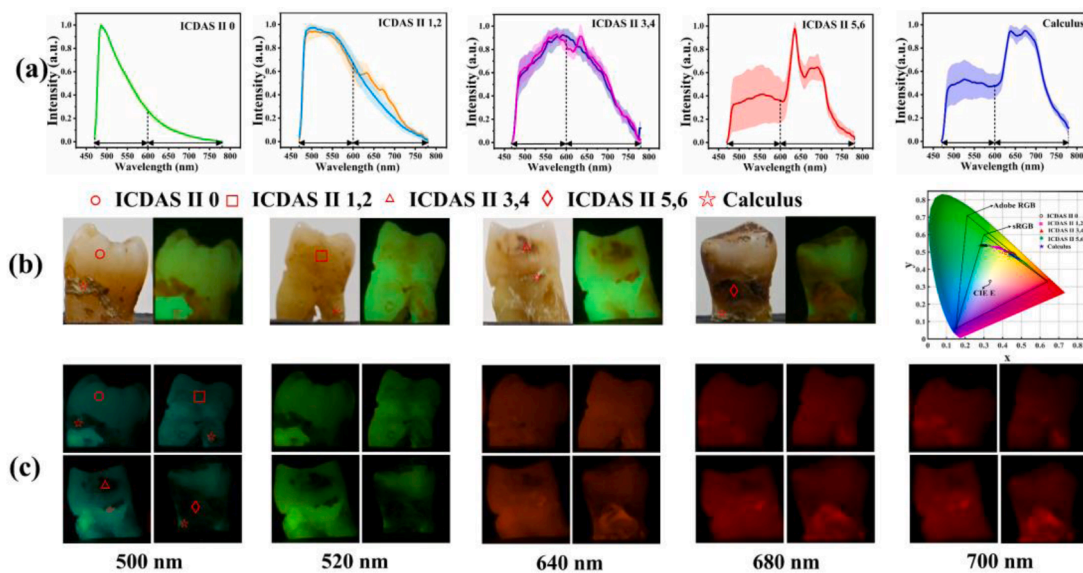


Fig. 2. Feature analysis, (a) Average fluorescence spectra of 500 POIs with four caries stages and calculus (after normalization, solid line) along with standard deviation (shaded area), (b) White light RGB images and fluorescent RGB images of four caries stages and calculus, and the distribution of 500 POIs by chromaticity coordinates in the CIE 1931 chromaticity diagram, (c) Fluorescence images in characteristic bands acquired by hyperspectral cameras.

segmentation methods to select a certain gray level to segment the target of interest from the image [37,38]. Gabor texture features were widely used as a visual cue for image analysis [39]. All data pre-processing was performed with matlab2020a software.

2.4. Feature fusion and machine learning algorithms

Conventional HSI classification methods utilize the spectral features of a single pixel without considering the spatial relationships of neighboring pixels [40]. Given the refinement requirements for caries and calculus identification, the spectrum, texture, and color features are fused and applied for classification features. To better demonstrate the performance of the fusion features, we performed ablation study and comparison with other methods. Four traditional nonlinear supervised machine learning algorithms, including Integrated Learning, Support Vector Machine (SVM), Decision Trees (DT), and Neural Networks, were used as classification algorithms in the model training phase. The performance of four machine learning algorithms is compared and evaluated to select the most suitable algorithm.

2.5. Model assessment

Accuracy, sensitivity, and specificity were important indexes to estimate model performance. The more effective the diagnosis was, the model's accuracy, specificity, and sensitivity was closer to 1. The parameters were calculated as follows:

$$ACC = \frac{(TP + TN)}{(P + N)} = \frac{(TP + TN)}{(TP + FN + TN + FP)} \quad (1)$$

$$TPR = \frac{TP}{P} = \frac{TP}{TP + FN} \quad (2)$$

$$TNR = \frac{TN}{N} = \frac{TN}{TN + FP} \quad (3)$$

where *ACC*, *TPR*, and *TNR* represent Accuracy, True Positive Rate (sensitivity), and True Negative Rate (specificity), respectively. *P* and *N* represent the actual positive sample quantity and the actual negative sample quantity. *TP* and *TN* represent True Positive and True Negative, which is the sample quantity correctly diagnosed as positive and correctly diagnosed as negative. *FP* and *FN* represent False Positive and False Negative, which is the sample quantity wrongly diagnosed as positive and quantity wrongly diagnosed as negative. Confusion matrixes were used as visual model evaluation tools. The accuracy was obtained from the validation set and the test set. Sensitivity, specificity, and confusion matrix were only from the test set.

3. Results and discussion

3.1. Feature analysis

Spectra and colors are frequently used as features in evaluating and diagnosing caries and calculus in QLF or LF techniques [16,22,27]. The original data set contains five disease categories, ICDAS II 0, ICDAS II 1, 2, ICDAS II 3,4, ICDAS II 5,6, and calculus. 100 POIs were randomly selected from each category, and each POI contained 311 pixel-valued intensities. Fig. 2(a) indicates that the average fluorescence spectra and variance were calculated for each category after normalization according to the maximum value. Healthy tooth enamel produces an intense emission peak around 480 nm due to the fluorophore it contains inside. With the progression of caries, the enamel structure is gradually destroyed, which leads to a decrease in incident light absorption and an increase in scattering. Based on the above two effects, the peak of the fluorescence spectrum around 480 nm decreases continuously. The content of bacteria and its metabolite porphyrins is accumulated with the development of caries, and one or two increasing emission peaks are

observed in the range of 600–700 nm. The calculus is formed by calcification of dental plaque, which also contains numerous porphyrins and therefore also forms two intense emission peaks between 600 and 700 nm. Plaque accumulation and calcification also attenuate the fluorescence intensity of tooth enamel near 480 nm. The spectra of ICDAS II 5,6 and calculus are very similar, with both fluorescence intensities diminishing in 480–599 nm and two strongly emitted peaks in 600–700 nm. Furthermore, the fluorescence spectra of a few ICDAS II 1,2 and ICDAS II 3,4 had no peak position of porphyrins in 600–700 nm, and the fluorescence intensity was only diminished in 470–599 nm, which may be caused by the short period for enamel mineralization to occur and for oral bacteria to synthesize porphyrins [17]. In practical applications, these phenomena may bring challenges to diagnosis using spectral features, while traditional spectrometers can only achieve single-point or single-area spectral acquisition, which is time-consuming and laborious.

Four different caries stages were selected for white light RGB images and fluorescent RGB images, as illustrated in Fig. 2(b). In the white light RGB images, the dental professional labeled the caries stages and areas based on ICDAS II standards. As caries progress, the Region of Interests (ROIs) in the fluorescent RGB images transit from green fluorescence (ICDAS II 0) of healthy enamel to red fluorescence (ICDAS II 5,6) of extensive cavities. However, visual changes in the color of early caries are not obvious and easily disturbed by pigmentation, light uniformity, and other factors. It is possible to have different caries stages and calculus on the same tooth surface. Fig. 2(b) shows that calculus was present on each tooth surface except for different caries stages. The color of the calculus and the caries are also not easy to distinguish. The fluorescence spectra of 500 POIs at different caries stages and calculus were transformed into 500 corresponding chromaticity coordinates in the CIE 1931 chromaticity diagram as presented in column 5 of Fig. 2(b). The trend of the color coordinates is consistent compared to the previous theoretical calculation work, with most of the coordinate points being within the commonly available color gamut region (sRGB and Adobe RGB) [34]. Because the filter used is not fully cut off at 470 nm, there is a slight drift in the color coordinates. There is no clear boundary between the color coordinates for different caries stages and calculus, especially the confusion between ICDAS II 3,4, ICDAS II 5,6, and calculus is obvious, consistent with the findings from direct viewing of fluorescent RGB images.

Characteristic band imaging is a form of visual representation with hyperspectral technology. Fig. 2(c) presents the images of 4 caries stages and calculus at five characteristic bands, including 500, 520, 640, 680, and 700 nm. These characteristic bands were selected based on the average and porphyrin bands reported in the literature [41]. The 500 and 520 nm bands can distinguish between normal enamel (ICDAS II 0) and infected areas (ICDAS II 1,2, ICDAS II 3,4, ICDAS II 5,6 and Calculus), but detailed 5-category delineation is not feasible. In the 640, 680, and 700 nm bands, ICDAS II 5,6 and calculus can be easily identified because their signal intensity is much larger than other surrounding tissues. Nevertheless, the difference between ICDAS II 0 and ICDAS II 1,2 is not significant, and neither is the distinction between calculus and ICDAS II 5,6 easy. In general, characteristic band imaging suffers from low manual recognition and cannot achieve 5 class division accurately.

Based on the above discussion, it is difficult to accurately and effectively distinguish different caries stages and calculus by a single spectrum or color feature in practical application. This work considers a fusion of spectral features, texture features, and color features as classification features, and their effectiveness is compared and verified in the following.

3.2. Model training process

As shown in Fig. 3, the model training process is divided into four steps: PCA dimensionality reduction, feature extraction, feature fusion, and model training. The spectral-image cube collected by the hyperspectral camera contains $m \times n$ spatial resolution and 311 spectral bands

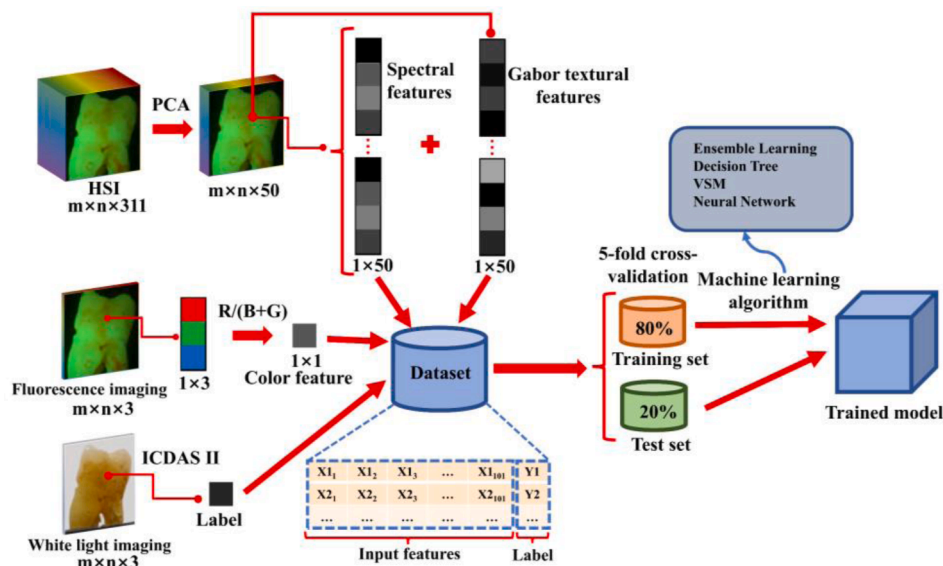


Fig. 3. Schematic diagram of the model training process.

(470–780 nm, 1 nm interval). The data volume of the spectral-image cube is too large, and PCA is first applied to the data cube for dimensionality reduction to reduce the complexity of the model. After PCA reduction, the performance of different spectral dimensions was tested with the model's accuracy as the evaluation index. The general trend is that the higher the spectral dimension, the better the accuracy rate. After calculation, when the spectral dimension is reduced to 50 dimensions, the accuracy of the model is close to that of the full spectrum (311 dimensions), but higher than that of 40 dimensions and 30 dimensions. The final choice of the data cube is $m \times n \times 50$, which reduces the data redundancy and retains the key feature information well. A total of three features are extracted, including spectral features, texture features, and color features. The POIs (size: 1×50) are extracted from the data cube after PCA dimensionality reduction as spectral features. The Gabor texture algorithm processes the $m \times n \times 50$ data cube, and then the POIs (size: 1×50) are extracted as texture features. The POIs (size: 1×3) are obtained from fluorescent RGB images (size: $m \times n \times 3$) and utilized as color features using the $R/(B + G)$ ratio method from the literature [18]. The label comes from the marking of professional physicians. There are 2420 POIs in the original dataset, and the input dataset is a 2420×102 feature matrix with the first 101 columns as feature vectors and 102 columns as label vectors. The 2420×102 feature matrix is named dataset A. The dataset B (size: 2420×101) has spectral features and texture features, and lacks color features. The dataset C (size: 2420×51) only has spectral features. Dataset A (spectral, texture and color features), dataset B (spectral and texture features) and dataset C (spectral features) were input to the model separately for training. Each dataset was randomly divided into 80% as the training set and 20% as the test set. Four traditional machine learning algorithms, including Integrated Learning, SVM, DT, and Neural Networks, were employed for model training to find a suitable classifier. 5-fold cross-validation was applied during the training.

3.3. Ablation study and comparison with other methods

Dataset A is trained with four algorithms to obtain models 1–4. Four algorithms train dataset B and dataset C to obtain models 5–8 and models 9–12. Hyperparameters optimization is one of the most difficult challenges in machine learning. Integrated learning, SVM, and DT are performed for 30 epochs, respectively. All models reach convergence after 30 epochs of training. Bayesian optimization is employed to find the best combination of hyperparameters to improve the model's

performance. The neural networks obtain the model with optimal performance by adjusting the number of fully connected layers, the number of neurons, and the excitation function. The optimal hyperparameter combinations and search ranges for each algorithm are in **supplemental document**. The training and test sets of each model are kept consistent and the training is completed in a very short time. The *ACC*, *TPR*, and *TNR* of each model on the test and validation sets are listed in **Table 2**. The accuracy of 12 models is relatively close on the validation and test sets, demonstrating that no significant overfitting is observed. The integrated learning algorithm has the highest *ACC*, *TPR*, and *TNR* of 98.6%, 98.4%, and 99.6% in dataset A with fused features. In dataset B and dataset C, the integrated learning algorithm also has the highest evaluation index. It can be seen that dataset A with fused features has higher accuracy, sensitivity, and specificity than dataset B and dataset C with the same machine learning algorithm. For example, model 1 outperforms model 5 and model 9, and model 4 outperforms model 8 and model 12. This indicates that the model can achieve better performance after fusing spectral, texture and color features. Compared to dataset C, which has only spectral features, dataset B fuses texture and spectral features, which can improve the accuracy of the model by approximately 2–3%. Dataset A with the fusion of three features gives another 1–2% improvement in model accuracy over dataset B. As listed in **Table 3**, the proposed method has advantages in terms of classifiability and accuracy compared to the results of other methods and enables the diagnosis of four caries stages and calculus.

The confusion matrixes are used as visualization tools to evaluate the classification effectiveness of the trained models. The confusion matrixes of the 12 trained models on the test set are presented in **Fig. 4**. The test set contains 485 POIs in 5 categories (ICDAS II 0, ICDAS II 1,2, ICDAS II 3,4, ICDAS II 5,6, and Calculus). The rows and columns in the confusion matrix represent the true and predicted labels, which can be seen concerning each other and the *TP*, *TN*, *FP*, and *FN* for each category. Among all 12 models, model 1 has the least prediction error. In dataset B and dataset C, model 5 and model 9 have high classification accuracy, but there are more classification errors between ICDAS II 1, 2 and ICDAS II 3, 4. Based on the above results, it can be preliminary concluded that feature fusion combined with an integrated learning algorithm can achieve the best results in the caries stage and calculus diagnosis. Due to the small training samples and the close evaluation indexes among the models, the generalization ability of the models is further verified in **Section 3.5**.

Table 2
Ablation study: accuracy, sensitivity, and specificity of the trained model.

Dataset	Model	Algorithm	Accuracy/% (ACC)		Sensitivity/% (TPR)	Specificity/% (TNR)
			Validation sets	Test sets	Test sets	Test sets
Dataset A (spectral, texture and color features)	Model 1	Integrated Learning	97.5	98.6	98.4	99.6
	Model 2	VSM	95.2	97.9	97.8	99.5
	Model 3	DT	95.3	97.1	97.0	99.3
	Model 4	Neural Networks	95.8	97.7	97.7	99.4
Dataset B (spectral and texture features)	Model 5	Integrated Learning	96.1	96.7	96.7	99.2
	Model 6	VSM	95.2	96.5	96.7	99.1
	Model 7	DT	91.9	94.0	93.8	98.5
	Model 8	Neural Networks	94.4	96.5	96.4	99.1
Dataset C (spectral features)	Model 9	Integrated Learning	94.4	95.3	95.3	98.8
	Model 10	VSM	90.4	93.2	93.0	98.3
	Model 11	DT	91.3	90.5	90.2	97.7
	Model 12	Neural Networks	91.8	92.6	92.4	98.2

Table 3
Comparison of the diagnostic effects (accuracy) of different methods for caries and calculus.

Number	Detection method	Diagnostic Category	Accuracy (ACC)%
1	Panoramic radiographs and deep learning [42]	2-classes (caries and non-caries)	87.0%
2	Panoramic films and deep learning [43]	3-classes (dentin lesions in the outer, middle, or inner third D1/2/3 of dentin)	95.7%
3	Bitewing images and deep learning [44]	3-classes (restorations, caries and normal)	90.3%
4	Smartphone images and machine learning [45]	3-classes (no surface change, visually non-cavitated, cavitated)	92.4%
5	Near-infrared (NIR) hyperspectral imaging and multiple discriminant analysis [28]	5-classes (enamel, dentin, calculus, enamel caries, dentin caries)	86.3%
6	Ours	5-classes (ICDAS II 0, ICDAS II 1,2, ICDAS II 3,4, ICDAS II 5,6, and calculus)	98.6%

3.4. Prediction process

The trained model enables accurate assessment and diagnosis of caries stages and calculus at the pixel point level on the tooth surface. The prediction process includes data acquisition, pre-processing, feature extraction, feature fusion, and result prediction, as shown in Fig. 5. First, the hyperspectral camera acquires an $m \times n \times 311$ image cube of the tooth surface. The image cube is pre-processed, including ROI extraction and PCA dimensionality reduction. The ROI extraction is based on the Otsu thresholding segmentation algorithm, which binarizes the image. The size of the image cube after PCA dimensionality reduction is $m1 \times n1 \times 50$. The 50-dimensional spectral features are extracted directly from the image cube. Then after Gabor algorithm processing, 50-dimensional texture features are extracted. Obtain color features from fluorescent RGB images. The spectral features, texture features, and color features are fused and input into the trained model as classification features to obtain classification results. The result of the model output is a pseudo-color image of the tooth surface labeled by a set of custom color maps. The five different colors indicate different caries stages and calculus, as indicated in Fig. 5. Contrast and discrimination enhancement of images is achieved by outputting pseudo color maps labeled with custom color maps. Different caries stages and calculus may exist on the same tooth surface, as shown in Fig. 5, and some tiny areas are not easily distinguished and identified on the fluorescent RGB images. The diagnostic model based on hyperspectral fluorescence imaging combined with a machine learning approach can realize pixel-level

classification, conducive to the accurate diagnosis of caries stages and calculus.

3.5. Enhanced recognition and quantitative assessment

The evaluation indexes (ACC, TPR, TNR) of the twelve trained models are obtained only on a small number of validation and test sets, and further validation and comparison of the generalization ability of the twelve models are needed on larger and more diverse data sets. A model with strong generalization capability means that high accuracy classification of larger sample datasets can be obtained by machine learning of small sample datasets. Five tooth surfaces with different caries stages and calculus are selected, and these tooth surfaces are not used in the previous training. The five tooth surfaces are named S1-S5, respectively. S3 has two caries stages. S4 and S5 have both caries and calculus, as shown in Fig. 6. As listed in Table 4, the ROIs of each tooth surface image after binarization processing also have about 40,00-pixel points, significantly larger than the validation and test sets. S1-S5 is evaluated and diagnosed by twelve trained models for caries stages and calculus, and pseudo-color maps are output. Models 1–4 represent the combination of fused features and machine learning algorithms, models 5–8 are obtained by combining spectral, texture features and machine learning algorithms, and models 9–12 are acquired with the combination of spectral and machine learning algorithms.

Fig. 6 shows the pseudo-color maps predicted by different models for the fluorescent RGB images with labels. Pixel points on a tooth surface image should usually show a block-like class distribution, meaning neighboring pixel points are most likely to be of the same class. As seen in Fig. 6(a)–(e), the same results are obtained as those in Section 3.3. Model 1 provides the best prediction results with clear boundaries, fewer false predictions, and blocky class distribution. Models 2–4 are susceptible to a wide range of misclassification in the boundary region, as shown in Fig. 6(a)–(b). Models 5–12 are easy to misclassify in the boundary regions and do not have a block-like class distribution. Model 1 and Model 5 are the two best-performing models using integrated learning algorithms, but Model 1 is superior to Model 5. As shown in Fig. 6(c), for the prediction of S3, model 5 does not distinguish well between ICDAS II 1,2 and ICDAS II 3,4, which is consistent with its previous performance in the confusion matrix. In general, Model 1, built based on feature fusion combined with integrated learning algorithms, is demonstrated to provide the optimal caries stage and calculus assessment and diagnosis.

In addition to the enhanced discrimination, model 1 provides a quantitative parameter, as listed in Table 4, which calculates the proportion of each lesion to the tooth surface area. For S1, 97.5% of areas of the tooth surface are classified as healthy enamel, and only 2.5% areas are classified as ICDAS II 1,2, which is almost consistent with the visual label of the specialist. S2, labeled as early caries, has about 8.9% of the tooth surface area classified as ICDAS II 1,2. Multiple disease classes

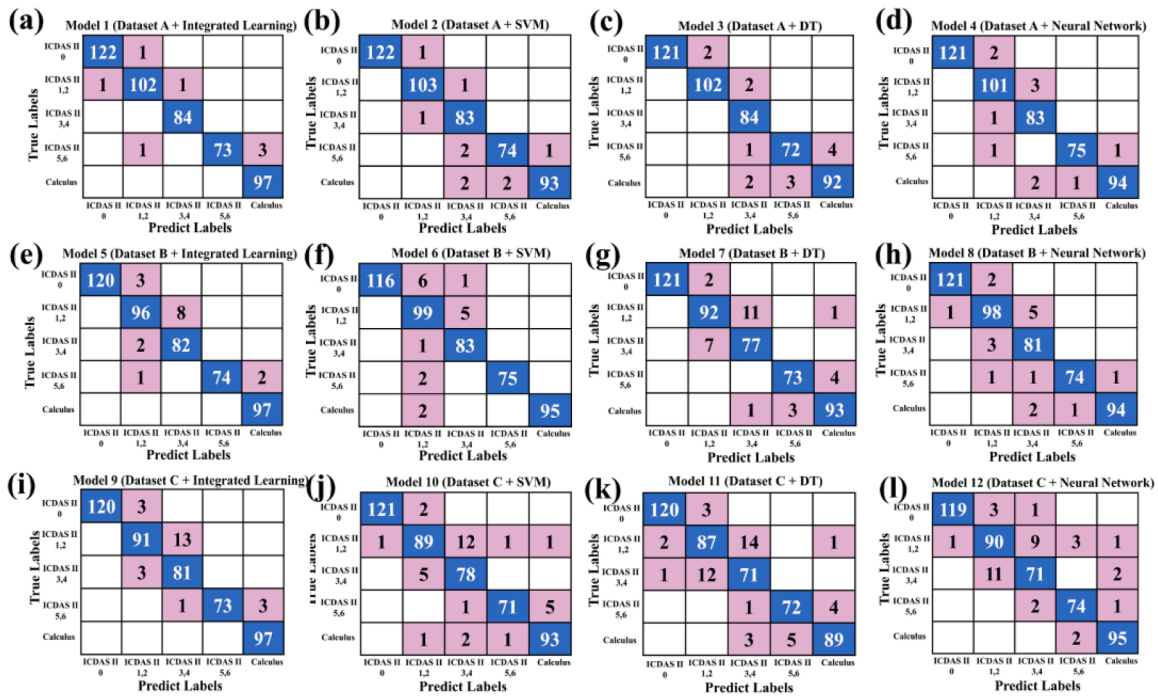


Fig. 4. Confusion matrix of 12 trained models on the test set.

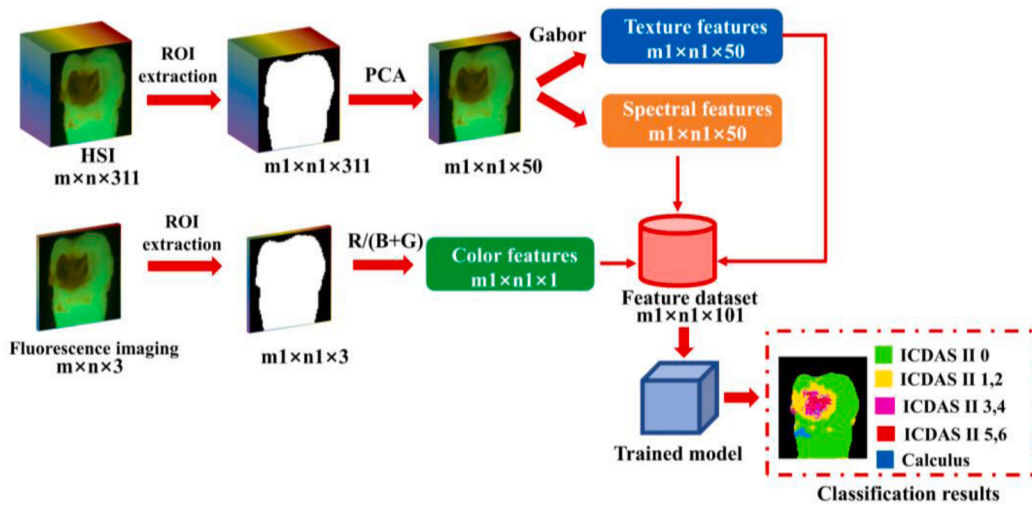


Fig. 5. Prediction process of the model and recognition enhancement.

exist on the same dental surface for S3–S5, and Model 1 can accurately identify and give the percentage of each category, thereby achieving a more refined assessment.

3.6. Potential application of the proposed method

High prevalence and low treatment rates are the main existing challenges for dental caries prevention and treatment [46]. Traditional visual, palpation, and radiological techniques for early caries detection have the risk of missing the diagnosis and are labor-intensive and time-consuming. The proposed method facilitates the development of supplementary clinical diagnostic tool and also relieves strained medical resources. In addition, due to the high prevalence and limited medical resources, the treatment rate of dental caries is low, especially in the regions with limited medical resources, many caries develops to root canal treatment or even tooth extraction due to the lack of timely

detection. Although the clinician can detect most caries by visual examination, it is difficult for the general population without a professional medical background. Therefore, the development of community and home caries automatic screening tool can promote the daily screening and detection of dental caries. The proposed method has the advantages of automatic, rapid, objective, and accurate, which can be useful for the development of community and home caries screening tool. Given the expensive price of hyperspectral equipment, the translation of the proposed method into a small handheld multispectral device or a screening tool that can be embedded in a smartphone is our future research direction.

4. Conclusion

Single-point spectroscopy is time-consuming and laborious in identifying caries and calculus using QLF or LF. The color differences

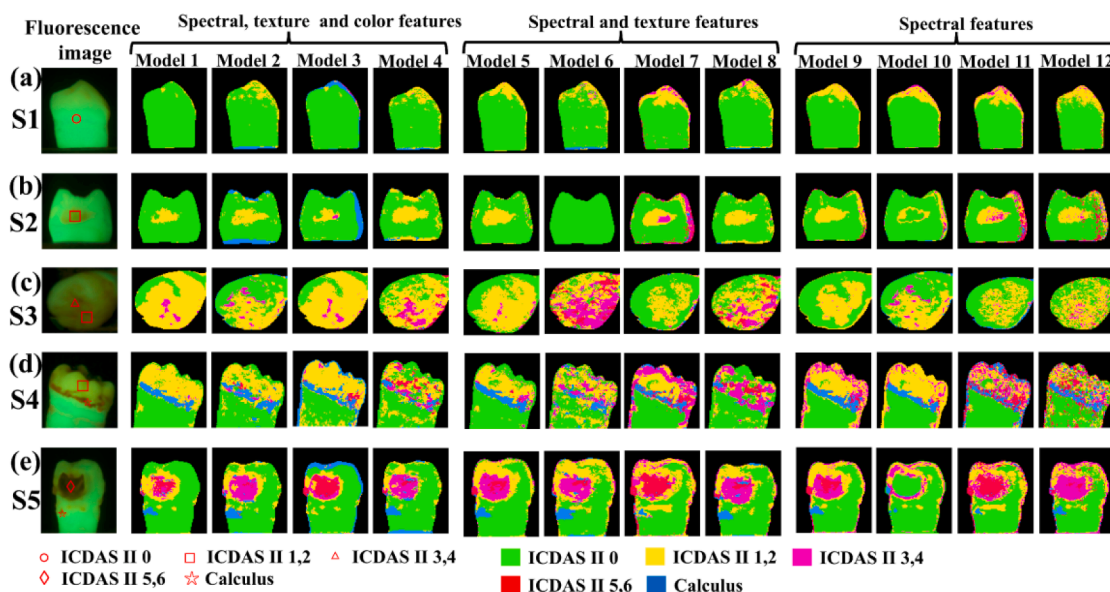


Fig. 6. Comparison of the generalization ability of 12 models.

Table 4
Quantitative parameters of tooth surfaces for caries stages and calculus.

Tooth surface	Number of pixel dots on the tooth surface	Number of pixel dots (ratio) (ICDAS II 0)	Number of pixel dots (ratio) (ICDAS II 1,2)	Number of pixel dots (ratio) (ICDAS II 3,4)	Number of pixel dots (ratio) (ICDAS II 5,6)	Number of pixel dots (ratio) (Calculus)
S1	4751	4630 (97.5%)	121 (2.5%)	0 (0%)	0 (0%)	0 (0%)
S2	3317	3022 (91.1%)	295 (8.9%)	0 (0%)	0 (0%)	0 (0%)
S3	4847	912 (18.8%)	3732 (77%)	203 (4.2%)	0 (0%)	0 (0%)
S4	4671	2329 (49.9%)	1853 (39.7%)	26 (0.5%)	24 (0.5%)	439 (9.4%)
S5	4559	3155 (69.2%)	863 (18.9%)	194 (4.3%)	223 (4.9%)	124 (2.7%)

between caries stages and calculus are difficult to distinguish, and the characteristic band imaging is difficult to classify accurately. The fusion features based on spectra, textures, and colors utilize both the spectral features of a single-pixel point and consider its neighborhood information. Compared to SVM, DT, and neural network algorithms, the model built with an integrated learning algorithm has better ACC, TPR, and TNR. Combining fused features and integrated learning can train a model with better evaluation indexes (ACC: 98.6%, TPR: 98.4%, TNR: 99.6%) and stronger generalization ability. The diagnostic model provides pixel-level caries and calculus assessment of the entire tooth surface while enabling discrimination enhancement and parameter quantification. The objective, accurate and rapid method for automatic identification of caries stages and calculus has potential applications in clinical, community, and family caries diagnosis and screening.

Data availability statement

The data that support the findings of this study are available on request from the corresponding author. The data are not publicly available due to privacy or ethical restrictions.

CRedit authorship contribution statement

Cheng Wang: Conceptualization, Methodology, Formal analysis, Investigation, Visualization, Writing – original draft. **Rongjun Zhang:** Supervision, Project administration. **Xiaoling Wei:** Validation, Resources, Funding acquisition. **Le Wang:** Formal analysis, Data curation. **Wenqian Xu:** Formal analysis, Data curation. **Qi Yao:** Conceptualization, Validation, Writing – review & editing, Supervision, Project administration, Funding acquisition.

Declaration of Competing Interest

There are no conflicts to declare.

Acknowledgments

This work was financially supported by State Key Laboratory of Applied Optics [SKLAO2021001A16]; Jihua Laboratory Projects of Guangdong Province [X190111UZ190]; Medical Engineering Fund of Fudan University [yg2021-028].

Supplementary materials

Supplementary material associated with this article can be found, in the online version, at doi:10.1016/j.pdpdt.2022.103217.

References

- [1] M.A. Peres, L.M.D. Macpherson, R.J. Weyant, B. Daly, R. Venturelli, M.R. Mathur, S. Listl, R.K. Celeste, C.C. Guarnizo-Herreño, C. Kearns, H. Benzian, P. Allison, R. G. Watt, Oral diseases: a global public health challenge, *Lancet N. Am. Ed.* 394 (2019) 249–260, [https://doi.org/10.1016/S0140-6736\(19\)31146-8](https://doi.org/10.1016/S0140-6736(19)31146-8).
- [2] P.E. Petersen, *The world oral health report 2003: continuous improvement of oral health in the 21st century - the approach of the WHO global oral health programme: the world oral health report 2003*, *Commun. Dent. Oral Epidemiol.* 31 (2003) 3–24.
- [3] J.E. Frencken, P. Sharma, L. Stenhouse, D. Green, D. Laverty, T. Dietrich, Global epidemiology of dental caries and severe periodontitis - a comprehensive review, *J. Clin. Periodontol.* 44 (2017) S94–S105, <https://doi.org/10.1111/jcpe.12677>.
- [4] S. Gonchukov, T. Biryukova, A. Sukhinina, Yu. Vdovin, Fluorescence detection of dental calculus, *Laser Phys. Lett.* 7 (2010) 812–816, <https://doi.org/10.1002/lapl.201010065>.

- [5] O.H. Tung, S.Y. Lee, Y.L. Lai, H.F. Chen, Characteristics of subgingival calculus detection by multiphoton fluorescence microscopy, *J. Biomed. Opt.* 16 (2011), 066017, <https://doi.org/10.1117/1.3593150>.
- [6] R.H. Selwitz, A.I. Ismail, N.B. Pitts, Dental caries, *Lancet N. Am. Ed.* 369 (2007) 52–59.
- [7] A. Akcali, N.P. Lang, Dental calculus: the calcified biofilm and its role in disease development, *J. Periodontology* 76 (1) (2000) 109–115, <https://doi.org/10.1111/prd.12151>, 2018.
- [8] N.B. Pitts, D.T. Zero, P.D. Marsh, K. Ekstrand, J.A. Weintraub, F. Ramos-Gomez, J. Tagami, S. Twetman, G. Tsakos, A. Ismail, Dental caries, *Nat. Rev. Dis. Primers* 3 (2017) 17030, <https://doi.org/10.1038/nrdp.2017.30>.
- [9] S.A. Son, K.H. Jung, C.C. Ko, Y.H. Kwon, Spectral characteristics of caries-related autofluorescence spectra and their use for diagnosis of caries stage, *J. Biomed. Opt.* 21 (2016), 015001, <https://doi.org/10.1117/1.JBO.21.1.015001>.
- [10] H.S. Chen, T.T. Chang, Color conversion technology of four-primary color images developed on wide color gamut red, green, blue monitor, *J. Imaging Sci. Technol.* 53 (2009), 060502, <https://doi.org/10.2352/J.ImagingSci.Technol.2009.53.6.060502>.
- [11] N. Abogazalah, M. Ando, Alternative methods to visual and radiographic examinations for approximal caries detection, *J. Oral Sci.* 59 (2017) 315–322, <https://doi.org/10.2334/josnusd.16-0595>.
- [12] N. Miyamoto, T. Adachi, F. Boschetto, M. Zanocco, T. Yamamoto, E. Marin, S. Somekawa, R. Ashida, W. Zhu, N. Kanamura, I. Nishimura, G. Pezzotti, Molecular fingerprint imaging to identify dental caries using Raman spectroscopy, *Materials* 13 (2020) 4900, <https://doi.org/10.3390/ma13214900>.
- [13] Y.H. El-Sharkawy, S. Elbasaney, Tunable laser-induced fluorescence with signal correlation algorithm for dental caries detection with controlled ablation, *Opt. Laser Technol.* 129 (2020), 106299, <https://doi.org/10.1016/j.optlastec.2020.106299>.
- [14] P. Wilder-Smith, J. Holtzman, J. Epstein, A. Le, Optical diagnostics in the oral cavity: an overview: optical diagnostics in the oral cavity: an overview, *Oral Dis.* 16 (2010) 717–728, <https://doi.org/10.1111/j.1601-0825.2010.01684.x>.
- [15] H.-E. Kim, B.-I. Kim, Early caries detection methods according to the depth of the lesion: an in vitro comparison, *Photodiagn. Photodyn. Ther.* 23 (2018) 176–180, <https://doi.org/10.1016/j.pdpdt.2018.06.014>.
- [16] B. Joseph, C.S. Prasanth, J.L. Jayanthi, J. Presanthila, N. Subhash, Detection and quantification of dental plaque based on laser-induced autofluorescence intensity ratio values, *J. Biomed. Opt.* 20 (2015), 048001, <https://doi.org/10.1117/1.JBO.20.4.048001>.
- [17] S.-A. Son, K.-H. Jung, C.-C. Ko, Y.H. Kwon, Spectral characteristics of caries-related autofluorescence spectra and their use for diagnosis of caries stage, *J. Biomed. Opt.* 048001 (21) (2016), <https://doi.org/10.1117/1.JBO.21.1.015001>.
- [18] Q.G. Chen, H.H. Zhu, Y. Xu, B. Lin, H. Chen, Quantitative method to assess caries via fluorescence imaging from the perspective of autofluorescence spectral analysis, *Laser Phys.* 25 (2015), 085601, <https://doi.org/10.1088/1054-660X/25/8/085601>.
- [19] M.A.I. Timoshchuk, J.S. Ridge, A.L. Rugg, L.Y. Nelson, A.S. Kim, E.J. Seibel, Real-Time Porphyrin Detection in Plaque and Caries: A Case Study, in: P. Rechmann, D. Fried (Eds.), San Francisco, California, United States, 2015, p. 93060C, <https://doi.org/10.1117/12.2081016>.
- [20] H. Bahramian, P. Argani, A. Baghalian, Comparison of different diagnostic techniques in detecting smooth surface caries in primary molars using the histological gold standard: an in vitro study, *Photodiagn. Photodyn. Ther.* 31 (2020), 101867, <https://doi.org/10.1016/j.pdpdt.2020.101867>.
- [21] A. Ribeiro, C. Rousseau, J. Girkin, A. Hall, R. Strang, C. John Whitters, S. Creanor, A.S.L. Gomes, A preliminary investigation of a spectroscopic technique for the diagnosis of natural caries lesions, *J. Dent.* 33 (2005) 73–78, <https://doi.org/10.1016/j.jdent.2004.08.006>.
- [22] Q. Chen, H. Zhu, Y. Xu, B. Lin, H. Chen, Discrimination of dental caries using colorimetric characteristics of fluorescence spectrum, *Caries Res.* 49 (2015) 401–407, <https://doi.org/10.1159/000381961>.
- [23] P.T.H. Mien, N.D. Khanh, N.T. Hao, H.T.H. Vy, D.N.K. Vy, T. Van Tien, H.Q. Linh, Design and manufacture of supporting device for detection of dental caries using fluorescence technique, in: Proceedings of the International Conference on Biomedical Engineering (BME-HUST), Hanoi, Vietnam, IEEE, 2016, pp. 85–89, <https://doi.org/10.1109/BME-HUST.2016.7782102>.
- [24] B. Dikmen, ICDAS II criteria (international caries detection and assessment system), *J. Istanbul. Univ. Fac. Dent.* 49 (2015) 63, <https://doi.org/10.17096/jiufd.38691>.
- [25] A. Jablonski-Momeni, D.N.J. Ricketts, K. Weber, O. Ziomek, M. Heinzl-Gutenbrunner, H.M. Schipper, R. Stoll, K. Pieper, Effect of different time intervals between examinations on the reproducibility of ICDAS-II for occlusal caries, *Caries Res.* 44 (2010) 191–195, <https://doi.org/10.1159/000314674>.
- [26] M.A. Calin, S.V. Parasca, D. Savastru, D. Manea, Hyperspectral imaging in the medical field: present and future, *Appl. Spectrosc. Rev.* 49 (2014) 435–447, <https://doi.org/10.1080/05704928.2013.838678>.
- [27] A.L. Abdel Gawad, Y. El-Sharkawy, H.S. Ayoub, A.F. El-Sherif, M.F. Hassan, Classification of dental diseases using hyperspectral imaging and laser induced fluorescence, *Photodiagn. Photodyn. Ther.* 25 (2019) 128–135, <https://doi.org/10.1016/j.pdpdt.2018.11.017>.
- [28] P. Usenik, M. Bürmen, A. Fidler, F. Pernuš, B. Likar, Automated classification and visualization of healthy and diseased hard dental tissues by near-infrared hyperspectral imaging, *Appl. Spectrosc.* 66 (2012) 1067–1074, <https://doi.org/10.1366/11-06460>.
- [29] B.J. Erickson, P. Korfiatis, Z. Akkus, T.L. Kline, Machine learning for medical imaging, *Radiographics* 37 (2017) 505–515, <https://doi.org/10.1148/rg.2017160130>.
- [30] B. Song, S. Sunny, R.D. Uthoff, S. Patrick, A. Suresh, T. Kolar, G. Keerthi, A. Anbarani, P. Wilder-Smith, M.A. Kuriakose, P. Birur, J.J. Rodriguez, R. Liang, Automatic classification of dual-modality, smartphone-based oral dysplasia and malignancy images using deep learning, *Biomed. Opt. Express.* 9 (2018) 5318, <https://doi.org/10.1364/BOE.9.005318>.
- [31] S.-H. Hur, E.-Y. Lee, M.-K. Kim, S. Kim, J.-Y. Kang, J.S. Lim, Machine learning to predict distal caries in mandibular second molars associated with impacted third molars, *Sci. Rep.* 11 (2021) 15447, <https://doi.org/10.1038/s41598-021-95024-4>.
- [32] M. Hung, M.W. Voss, M.N. Rosales, W. Li, W. Su, J. Xu, J. Bounsanga, B. Ruiz-Negrón, E. Lauren, F.W. Licari, Application of machine learning for diagnostic prediction of root caries, *Gerodontology* 36 (2019) 395–404, <https://doi.org/10.1111/ger.12432>.
- [33] P. Francescut, B. Zimmerli, A. Lussi, Influence of different storage methods on laser fluorescence values: a two-year study, *Caries Res.* 40 (2006) 181–185, <https://doi.org/10.1159/000092223>.
- [34] C. Wang, R. Zhang, Y. Jiang, J. Li, N. Liu, L. Wang, P. Wu, J. He, Q. Yao, X. Wei, Fluorescence spectrometry based chromaticity mapping, characterization, and quantitative assessment of dental caries, *Photodiagn. Photodyn. Ther.* (2022), 102711, <https://doi.org/10.1016/j.pdpdt.2021.102711>.
- [35] H. Erives, N.B. Targhetta, Implementation of a 3-D hyperspectral instrument for skin imaging applications, *IEEE Trans. Instrum. Meas.* 58 (2009) 631–638, <https://doi.org/10.1109/TIM.2009.2005557>.
- [36] X. Kang, X. Xiang, S. Li, J.A. Benediktsson, PCA-based edge-preserving features for hyperspectral image classification, *IEEE Trans. Geosci. Remote Sens.* 55 (2017) 7140–7151, <https://doi.org/10.1109/TGRS.2017.2743102>.
- [37] C. Lu, P. Zhu, Y. Cao, The segmentation algorithm of improvement a two-dimensional Otsu and application research, in: Proceedings of the 2nd International Conference on Software Technology and Engineering, San Juan, PR, USA, IEEE, 2010, 5608908, <https://doi.org/10.1109/ICSTE.2010.5608908>.
- [38] N. Otsu, A threshold selection method from gray-level histograms[J], *Automatica* 11 (1975) 285–296, <https://doi.org/10.1109/TSMC.1979.4310076>.
- [39] F. Riaz, A. Hassan, S. Rehman, U. Qamar, Texture classification using rotation- and scale-invariant gabor texture features, *IEEE Signal Process. Lett.* 20 (2013) 607–610, <https://doi.org/10.1109/LSP.2013.2259622>.
- [40] Y. Li, L. Deng, X. Yang, Z. Liu, X. Zhao, F. Huang, et al., Early diagnosis of gastric cancer based on deep learning combined with the spectral-spatial classification method, *Biomed. Opt. Express.* 10 (2019) 4999, <https://doi.org/10.1364/BOE.10.004999>.
- [41] S.P. Singh, P. Fält, I. Barman, A. Koistinen, R.R. Dasari, A.M. Kullaa, Objective identification of dental abnormalities with multispectral fluorescence imaging, *J. Biophoton.* 10 (2017) 1279–1286, <https://doi.org/10.1002/jbio.201600218>.
- [42] S. Vinayahalingam, S. Kempers, L. Limon, D. Deibel, T. Maal, M. Hanisch, S. Bergé, T. Xi, Classification of caries in third molars on panoramic radiographs using deep learning, *Sci. Rep.* 11 (2021) 12609, <https://doi.org/10.1038/s41598-021-92121-2>.
- [43] L. Lian, T. Zhu, F. Zhu, H. Zhu, Deep learning for caries detection and classification, *Diagnostics* 11 (2021) 1672, <https://doi.org/10.3390/diagnostics11091672>.
- [44] Y.-C. Mao, T.-Y. Chen, H.-S. Chou, S.-Y. Lin, S.-Y. Liu, Y.-A. Chen, Y.-L. Liu, C.-A. Chen, Y.-C. Huang, S.-L. Chen, C.-W. Li, P.A.R. Abu, W.-Y. Chiang, Caries and restoration detection using bitewing film based on transfer learning with CNNs, *Sensors* 21 (2021) 4613, <https://doi.org/10.3390/s21134613>.
- [45] D.L. Duong, M.H. Kabir, R.F. Kuo, Automated caries detection with smartphone color photography using machine learning, *Health Inform. J.* 27 (2021), 146045822110075, <https://doi.org/10.1177/14604582211007530>.
- [46] L. Cheng, Expert consensus on dental caries management, *Int. J. Oral Sci.* 14 (1) (2022) 1–8.